

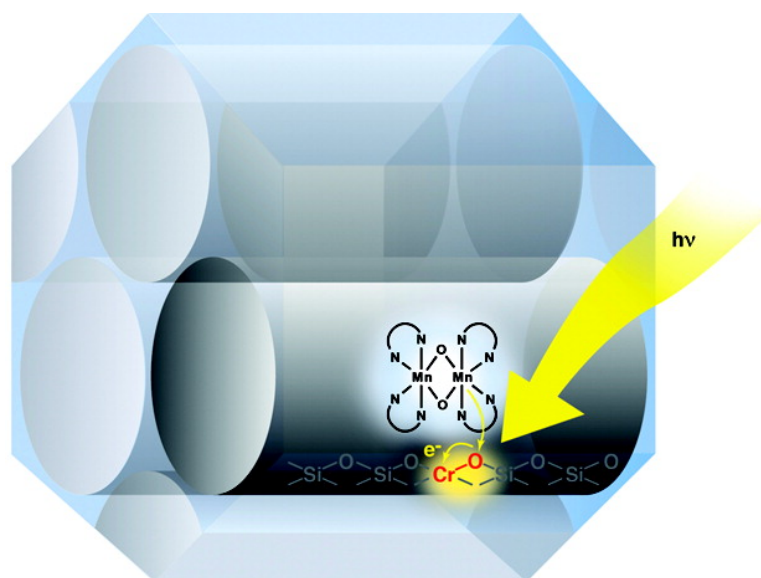
Article

Visible Light-Induced Electron Transfer from Di- μ -oxo-Bridged Dinuclear Mn Complexes to Cr Centers in Silica Nanopores

Walter W. Weare, Yulia Pushkar, Vittal K. Yachandra, and Heinz Frei

J. Am. Chem. Soc., **2008**, 130 (34), 11355-11363 • DOI: 10.1021/ja801546a • Publication Date (Web): 30 July 2008

Downloaded from <http://pubs.acs.org> on February 8, 2009



More About This Article

Additional resources and features associated with this article are available within the HTML version:

- Supporting Information
- Links to the 1 articles that cite this article, as of the time of this article download
- Access to high resolution figures
- Links to articles and content related to this article
- Copyright permission to reproduce figures and/or text from this article

[View the Full Text HTML](#)

Visible Light-Induced Electron Transfer from Di- μ -oxo-Bridged Dinuclear Mn Complexes to Cr Centers in Silica Nanopores

Walter W. Weare, Yulia Pushkar, Vittal K. Yachandra, and Heinz Frei*

Physical Biosciences Division, Lawrence Berkeley National Laboratory, University of California, Berkeley, California 94720

Received February 29, 2008; E-mail: HMFrei@lbl.gov

Abstract: The compound $(\text{bpy})_2\text{Mn}^{\text{III}}(\mu\text{-O})_2\text{Mn}^{\text{IV}}(\text{bpy})_2$, a structural model relevant for the photosynthetic water oxidation complex, was coupled to single Cr^{VI} charge-transfer chromophores in the channels of the nanoporous oxide AIMCM-41. Mn K-edge EXAFS spectroscopy confirmed that the di- μ -oxo dinuclear Mn core of the complex is unaffected when loaded into the nanoscale pores. Observation of the 16-line EPR signal characteristic of $\text{Mn}^{\text{III}}(\mu\text{-O})_2\text{Mn}^{\text{IV}}$ demonstrates that the majority of the loaded complexes retained their nascent oxidation state in the presence or absence of Cr^{VI} centers. The FT-Raman spectrum upon visible light excitation of the $\text{Cr}^{\text{VI}}\text{-O}^{\text{II}} \rightarrow \text{Cr}^{\text{V}}\text{-O}^{\text{I}}$ ligand-to-metal charge transfer reveals electron transfer from $\text{Mn}^{\text{III}}(\mu\text{-O})_2\text{Mn}^{\text{IV}}$ (Mn–O stretch at 700 cm^{-1}) to Cr^{VI} , resulting in the formation of Cr^{V} and $\text{Mn}^{\text{IV}}(\mu\text{-O})_2\text{Mn}^{\text{IV}}$ (Mn–O stretch at 645 cm^{-1}). All initial and final states are directly observed by FT-Raman or EPR spectroscopy, and the assignments are corroborated by X-ray absorption spectroscopy measurements. The endoergic charge separation products ($\Delta E_{\text{o}} = -0.6\text{ V}$) remain after several minutes, which points to spatial separation of Cr^{V} and $\text{Mn}^{\text{IV}}(\mu\text{-O})_2\text{Mn}^{\text{IV}}$ as a consequence of hole (O^{I}) hopping as a major contributing mechanism. This is the first observation of visible light-induced oxidation of a potential water oxidation complex by a metal charge-transfer pump in a nanoporous environment. These findings will allow for the assembly and photochemical characterization of well-defined transition metal molecular units, with the ultimate goal of performing endothermic, multielectron transformations that are coupled to visible light electron pumps in nanostructured scaffolds.

1. Introduction

Synthetic polynuclear manganese complexes have received much attention as candidates for water oxidation catalysts in engineered solar-to-chemical conversion systems due to the role of Mn in the water oxidation complex of Photosystem II.¹ While only a few dinuclear Mn complexes have been implicated in the evolution of O_2 when chemically driven by strong oxidants in solution^{2–4} or adsorbed on high-surface-area supports such as clays^{4–6} or nanoporous silica,⁷ the vast majority of such polynuclear Mn compounds have served as structural models for the natural water oxidation complex.^{8–12} These complexes

are also useful for the study of electron transfer between a Mn core and an electron acceptor. Understanding the photon-driven electron transfer in all such systems has proven essential for the continued development of artificial photosynthetic systems.^{13,14} For Mn-based systems, Magnuson et al. and Burdinski et al. have demonstrated photon-induced electron transfer from a dinuclear Mn complex to a covalently attached $\text{Ru}(\text{bpy})_3$; the latter functions as a charge-transfer pump by generating a transient Ru^{III} upon excitation of Ru^{II} in the presence of an acceptor in solution.^{15–17} Synthetic manipulation of the chemical nature, the mode of attachment, and the redox properties of the organic linkage between the Mn core and the Ru chromophore coupled with time-resolved optical spectroscopy of the systems has provided critical insights into the energetics and kinetics of

- (1) Yano, J.; Kern, J.; Sauer, K.; Latimer, M. J.; Pushkar, Y.; Biesiadka, J.; Loll, B.; Saenger, W.; Messinger, J.; Zouni, A.; Yachandra, V. K. *Science* **2006**, *314*, 821–825.
- (2) Chen, H.; Tagore, R.; Das, S.; Incarvito, C.; Faller, J. W.; Crabtree, R. H.; Brudvig, G. W. *Inorg. Chem.* **2005**, *44*, 7661–7670.
- (3) Chen, H.; Tagore, R.; Olack, G.; Vrettos, J. S.; Weng, T. C.; Penner-Hahn, J.; Crabtree, R. H.; Brudvig, G. W. *Inorg. Chem.* **2007**, *46*, 34–43.
- (4) Yagi, M.; Kaneko, M. *Chem. Rev.* **2001**, *101*, 21–35.
- (5) Yagi, M.; Narita, K. *J. Am. Chem. Soc.* **2004**, *126*, 8084–8085.
- (6) Narita, K.; Kuwabara, T.; Sone, K.; Shimizu, K.; Yagi, M. *J. Phys. Chem. B* **2006**, *110*, 23107–23114.
- (7) Rumberger, E. M. W.; Bell, A. T.; Tilley, T. D. Presented at the Symposium on Catalysis Relevant to Energy and Sustainability, 233rd ACS National Meeting, Chicago, March 2007.
- (8) Ruettinger, W.; Dismukes, G. C. *Chem. Rev.* **1997**, *97*, 1–24.
- (9) Manchanda, R.; Brudvig, G. W.; Crabtree, R. H. *Coord. Chem. Rev.* **1995**, *144*, 1–38.
- (10) Pecoraro, V. L.; Baldwin, M. J.; Gelasco, A. *Chem. Rev.* **1994**, *94*, 807–826.

- (11) Law, N. A.; Caudle, M. T.; Pecoraro, V. L. In *Advanced Inorganic Chemistry*; Academic Press: San Diego, 1999; Vol. 46.
- (12) Mukhopadhyar, S.; Mandal, S. K.; Beaduri, S.; Armstrong, W. H. *Chem. Rev.* **2004**, *104*, 3981–4026.
- (13) Gust, D.; Moore, T. A.; Moore, A. L. *Acc. Chem. Res.* **2001**, *34*, 40–48.
- (14) Morris, N. D.; Suzuki, M.; Mallouk, T. E. *J. Phys. Chem. A* **2004**, *108*, 9115–9119.
- (15) Sun, L. C.; Raymond, M. K.; Magnuson, A.; LeGourrierec, D.; Tamm, M.; Abrahamsson, M.; Kenez, P. H.; Martensson, J.; Stenhagen, G.; Hammarstrom, L.; Styring, S.; Akermark, B. *J. Inorg. Biochem.* **2000**, *78*, 15–22.
- (16) Borgstrom, M.; Shaikh, N.; Johansson, O.; Anderlund, M. F.; Styring, S.; Akermark, B.; Magnuson, A.; Hammarstrom, L. *J. Am. Chem. Soc.* **2005**, *127*, 17504–17515.
- (17) Burdinski, D.; Wieghardt, K.; Steenken, S. *J. Am. Chem. Soc.* **1999**, *121*, 10781–10787.

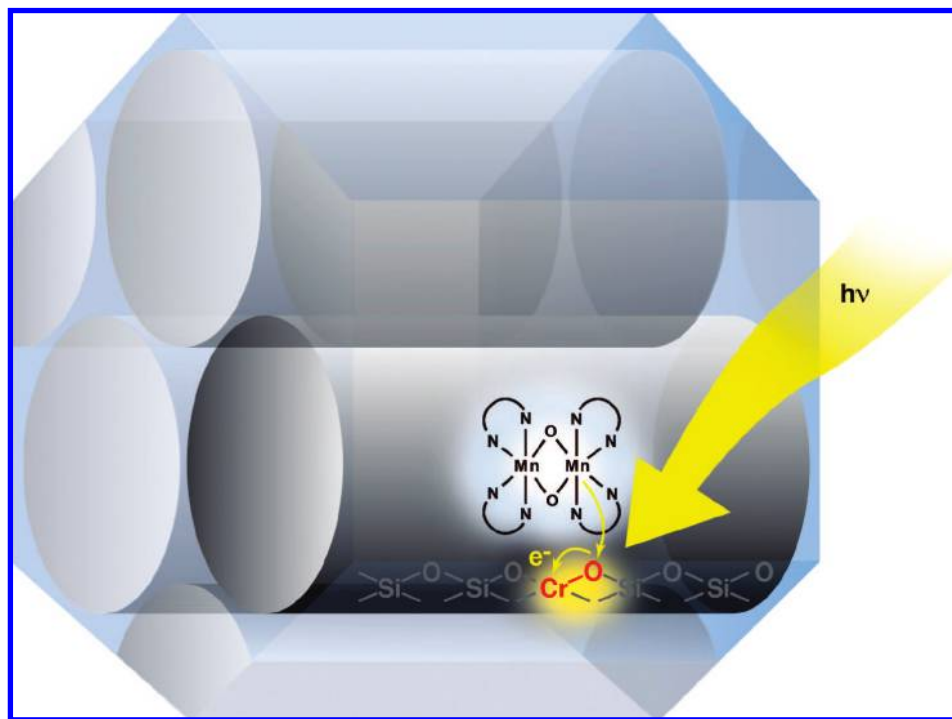


Figure 1. Schematic representation of the photon-induced electron-transfer reaction. Light excites a $\text{Cr}^{\text{VI}}\text{-O}$ LMCT, creating the high-energy intermediate that transfers an electron from $(\text{bpy})_2\text{Mn}^{\text{III}}(\mu\text{-O})_2\text{Mn}^{\text{IV}}(\text{bpy})_2$ into Cr^{VI} , creating Cr^{V} .

sequential light-driven transfer of electrons out of the Mn core. In such systems, as many as three sequential oxidation steps are observed, with $\text{Mn}^{\text{III}}\text{Mn}^{\text{IV}}$ being the highest oxidation state achieved for the Mn core to date.¹⁸ Knowledge of these physicochemical properties are key for optimizing the efficiency for visible light-driven water oxidation catalysis.

Inorganic molecular photocatalytic units that are arranged and coupled on inert nanoporous oxide supports offer opportunities for developing artificial systems for sunlight to chemical energy conversion. Our approach features photocatalytic units consisting of a single metal center or an oxo-bridged heterodinuclear charge-transfer group that absorbs visible light to generate transient oxidizing (or reducing) intermediates. These can then be linked to multielectron catalysts to achieve the desired reactivity. The photocatalytic units are covalently anchored on the surface of nanoporous silica materials, like MCM-41.^{19–23} Such high-surface-area oxide supports allow for a high density of reactive sites while retaining the independence of each site as unique chemical species. The nanostructured features also offer possibilities to arrange and couple photocatalytic oxidation and reduction sites in ways that instantly separate the redox products, minimizing back-reactions. The modular nature of such a system's polynuclear metal centers allows for optimization of several critical properties. These include redox level matches, visible light absorption characteristics, and efficient electronic coupling. We believe that the flexibility of this approach will eventually allow for the development of integrated sunlight-to-

fuel conversion systems where each component is coupled to another with minimal loss of energy or charge.

In recent work, we demonstrated visible light-induced oxidation of water using iridium oxide (IrO_2) nanoclusters coupled to single Cr^{VI} or $\text{TiOCr}^{\text{III}}$ charge-transfer pumps in MCM-41 silica nanopores.^{21,24} While this noble metal catalyst successfully oxidizes water, there is an urgent need for exploring Mn or other first row transition metal-based water oxidation catalysts because large-scale deployment of solar fuel conversion systems requires the use of inexpensive, abundant materials. Equally important, from a fundamental research standpoint, is the need to gain a detailed understanding of photon-induced charge-transfer processes between catalysts and visible light chromophores. Polynuclear transition metal complexes, as well-characterized molecular units, offer spectroscopic precision into chemical and electronic states at a level not readily attainable with metal oxide nanocluster catalysts.

In this paper, we report the coupling of molecular, bridging di- μ -oxo dinuclear Mn model catalysts, in particular $(\text{bpy})_2\text{Mn}^{\text{III}}(\mu\text{-O})_2\text{Mn}^{\text{IV}}(\text{bpy})_2$, to single Cr^{VI} charge-transfer pumps loaded inside the nanopores of the silica material AIMCM-41. Visible light-driven transfer of electrons from the Mn core to the chromophore is demonstrated, with the core reaching its highest, $\text{Mn}^{\text{IV}}(\mu\text{-O})_2\text{Mn}^{\text{IV}}$ oxidation state (Figure 1).

2. Results and Discussion

In the first part of this study, we focus on the structure and integrity of di- μ -oxo dinuclear Mn complexes upon loading into a nanoporous support (AIMCM-41, an aluminum-functionalized amorphous silica material with 30 Å cylindrical channels and a surface area of 1250 m^2/g).²⁵ This is followed by experiments

(18) Huang, P.; Magnuson, A.; Lomoth, R.; Abrahamsson, M.; Tamm, M.; Sun, L.; van Rotterdam, B.; Park, J.; Hammarstrom, L.; Akermark, B.; Styring, S. *J. Inorg. Biochem.* **2002**, *91*, 159–172.

(19) Lin, W.; Frei, H. *J. Phys. Chem. B* **2005**, *109*, 4929–4935.

(20) Lin, W.; Frei, H. *J. Am. Chem. Soc.* **2005**, *127*, 1610–1611.

(21) Han, H.; Frei, H. *J. Phys. Chem. C* **2008**, *112*, 8391–8399.

(22) Wu, X.; Han, H.; Frei, H., manuscript in preparation.

(23) Nakamura, R.; Okamoto, A.; Osawa, H.; Irie, H.; Hashimoto, K. *J. Am. Chem. Soc.* **2007**, *129*, 9596.

(24) Nakamura, R.; Frei, H. *J. Am. Chem. Soc.* **2006**, *128*, 10668–10669.

(25) Weckhuysen, B. M.; Wachs, I. E.; Schoonheydt, R. A. *Chem. Rev.* **1996**, *96*, 3327–3350.

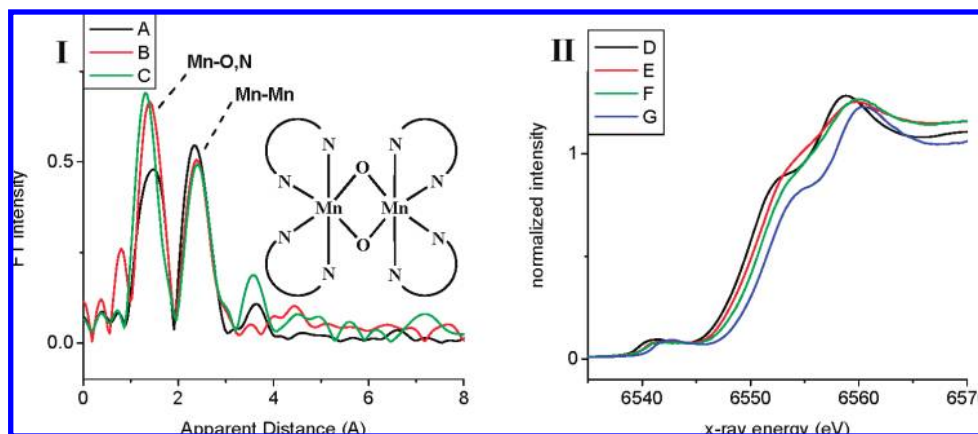


Figure 2. (I) FT of the k^3 -weighted Mn K-edge EXAFS of (A) crystalline $[(bpy)_2Mn^{III}(\mu-O)_2Mn^{IV}(bpy)_2](NO_3)_3$, (B) $(bpy)_2Mn^{III}(\mu-O)_2Mn^{IV}(bpy)_2$ loaded into AIMCM-41 (0.5 wt %), and (C) complex loaded into Cr-AIMCM-41 (Cr/Si = 0.01). (II) Mn K-edge XANES of (D) crystalline $[(bpy)_2Mn^{III}(\mu-O)_2Mn^{IV}(bpy)_2](NO_3)_3$, (E) $(bpy)_2Mn^{III}(\mu-O)_2Mn^{IV}(bpy)_2$ loaded into AIMCM-41 (0.5 wt %), (F) complex loaded into Cr-AIMCM-41, and (G) crystalline $[(Me_2-bpy)_2Mn^{IV}(\mu-O)_2Mn^{IV}(Me_2-bpy)_2][ClO_4]_4$. Traces D and G are included to reference the edge position of $Mn_2^{III/IV}$ and $Mn_2^{IV/IV}$, respectively.

Table 1. Mn K-Edge EXAFS Curve-Fitting Results for $(bpy)_2Mn^{III}(\mu-O)_2Mn^{IV}(bpy)_2$ Loaded into AIMCM-41 and Cr-AIMCM-41 and for Crystalline $[(bpy)_2Mn^{III}(\mu-O)_2Mn^{IV}(bpy)_2](NO_3)_3$

fit	sample, figure no.	shell	R (Å)	N (with $S_0^2 = 0.85$)	σ^2 ($\times 10^3$ Å ²)	Φ ($\times 10^3$)	ϵ^2 ($\times 10^5$)
1	pure, 1A	Mn–O	1.78	0.9	1	0.4	0.16
		Mn–N	2.10	2.3	13		
2	Mn ₂ on AIMCM, 1B	Mn–O	1.81	1.2	1.6	0.3	0.12
		Mn–N	2.15	2.2	12		
3	Mn ₂ on Cr-AIMCM, 1C	Mn–O	1.80	1.1	0.8	0.8	0.37
		Mn–N	2.08	2.7	25		
4	pure, 1A	Mn–Mn	2.73	0.6	2 ^a	0.6	0.28
5	Mn ₂ on AIMCM, 1B	Mn–Mn	2.72	0.5	2 ^a	0.4	0.19
6	Mn ₂ on Cr-AIMCM, 1C	Mn–Mn	2.74	0.5	2 ^a	0.6	0.28

^a Value fixed during minimization.

demonstrating that visible light drives the oxidation of the Mn core when coupled to a Cr^{VI} chromophore.

2.1. Characterization of $(bpy)_2Mn^{III}(\mu-O)_2Mn^{IV}(bpy)_2$ Loaded into Nanoporous Solid. Figure 2(I) shows the Fourier transform (FT) of the Mn K-edge EXAFS of $(bpy)_2Mn^{III}(\mu-O)_2Mn^{IV}(bpy)_2$ loaded into Cr-AIMCM-41 (Cr/Si = 0.007 according to ICP/MS) (trace C) and plain AIMCM-41 (trace B). The loading level of the complex is 0.5 wt % (corresponding to a Cr:Mn₂ ratio of 11:1). For comparison, the FT of crystalline $[(bpy)_2Mn^{III}(\mu-O)_2Mn^{IV}(bpy)_2](NO_3)_3$ is included as trace A of Figure 2(I). The results of Mn K-edge EXAFS curve fitting for the three samples are summarized in Table 1. No significant differences are found for the Mn–O and Mn–N distances (first FT peak of Figure 2(I)) as well as the Mn–Mn distance (second FT peak) for the complex inside Cr-AIMCM-41, AIMCM-41, or in crystalline form. Also, the coordination numbers of the three samples agree within uncertainties. The intense Mn–Mn FT peak of traces B and C clearly demonstrates that the majority of the complexes have intact di- μ -oxo Mn dinuclear cores inside the silica nanopores in the presence or absence of Cr centers. (At 20-fold higher concentration of the complex, curve fitting gives a second Mn–Mn distance of 2.98 Å, probably due to Mn cluster formation. Corresponding Mn K-edge EXAFS curve fitting results are presented in Table S1 of the Supporting Information.) The Mn K-edge XANES spectra of loaded $(bpy)_2Mn^{III}(\mu-O)_2Mn^{IV}(bpy)_2$ are similar to those of the reference compounds (Figure 2(II)) and change very little between AIMCM-41 and Cr-AIMCM-41. One noticeable effect is the broadening of the shoulder on the rising edge at ~ 6555 eV, which has previously been assigned to a Mn-to-ligand π^*

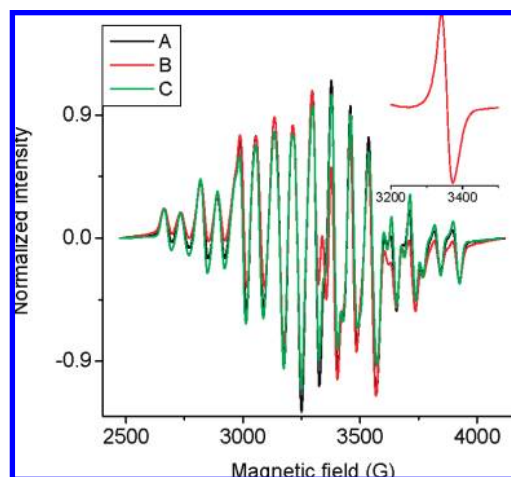


Figure 3. X-band EPR spectra of $(bpy)_2Mn^{III}(\mu-O)_2Mn^{IV}(bpy)_2$ loaded into (A) AIMCM-41, (B) Cr-AIMCM-41, and (C) $[(bpy)_2Mn^{III}(\mu-O)_2Mn^{IV}(bpy)_2](NO_3)_3$ in acetonitrile solution. Spectra were recorded at 20 K. The small signal at ~ 3300 G originates from the residual Cr^V present in Cr-AIMCM-41. Inset is an EPR spectrum of calcined Cr-AIMCM-41 for comparison.

transition.²⁶ This broadening implies that the bipyridine ligands become disordered when the dinuclear Mn complexes are

- (26) Visser, H.; Anxolabehere-Mallart, E.; Bergmann, U.; Glatzel, P.; Robblee, J. H.; Cramer, S. P.; Girerd, J.-J.; Sauer, K.; Klein, M. P.; Yachandra, V. K. *J. Am. Chem. Soc.* **2001**, *123*, 7031–7039.
 (27) Bajt, S.; Clark, S. B.; Sutton, S. R.; Rivers, M. L.; Smith, J. V. *Anal. Chem.* **1993**, *65*, 1800–1804.

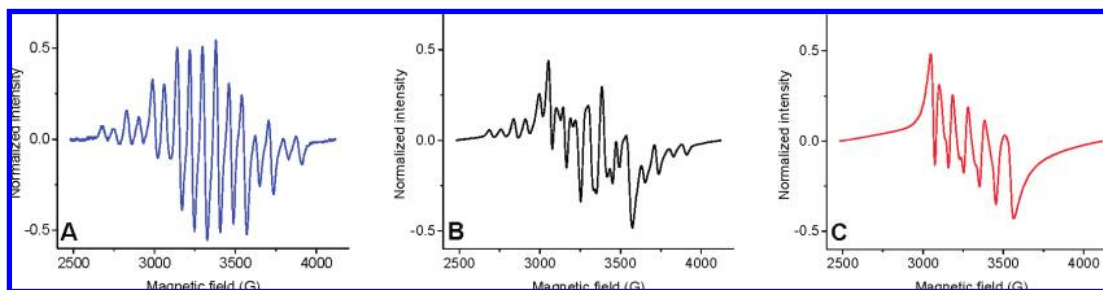


Figure 4. X-band EPR signal of AIMCM-41 loaded with 4 wt % $\text{terpy}_2\text{Mn}_2\text{O}_2$. The samples were kept under ambient conditions for (A) 10 min, (B) 6 h, and (C) 7 days after loading was complete and then frozen under liquid N_2 for EPR analysis. EPR intensities were arbitrarily normalized for comparison.

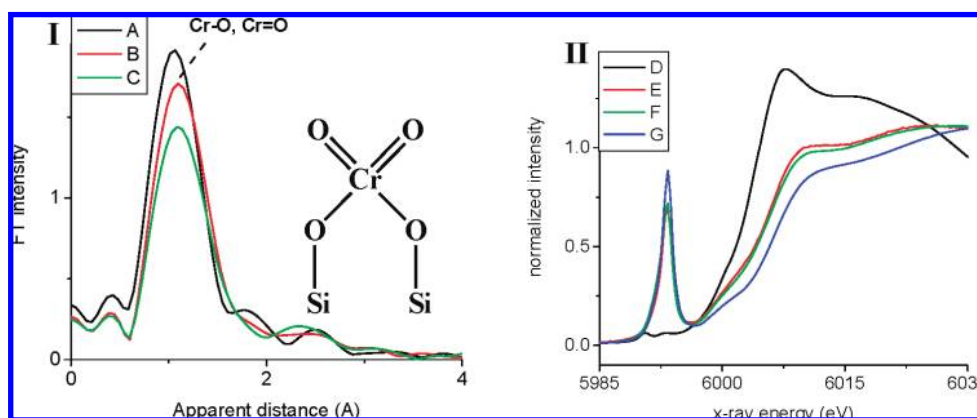


Figure 5. (I) FT of k^3 -weighted Cr K-edge EXAFS of (A) Cr-AIMCM-41, (B) Cr-AIMCM-41 loaded with 9.5 wt % $(\text{bpy})_2\text{Mn}^{\text{III}}(\mu\text{-O})_2\text{Mn}^{\text{IV}}(\text{bpy})_2$, and (C) Cr-AIMCM-41 loaded with 0.5 wt % $(\text{bpy})_2\text{Mn}^{\text{III}}(\mu\text{-O})_2\text{Mn}^{\text{IV}}(\text{bpy})_2$. (II) Cr K-edge XANES of (D) $\text{Cr}(\text{NO}_3)_3$ (solid Cr(III) compound), (E) Cr-AIMCM-41 treated with 0.01 M 2,2'-bipyridine, (F) Cr-AIMCM-41 loaded with 0.5 wt % $(\text{bpy})_2\text{Mn}^{\text{III}}(\mu\text{-O})_2\text{Mn}^{\text{IV}}(\text{bpy})_2$, and (G) calcined Cr-AIMCM-41.

Table 2. Cr K-Edge EXAFS Curve-Fitting Results for Cr-AIMCM-41, 0.5 wt % $(\text{bpy})_2\text{Mn}^{\text{III}}(\mu\text{-O})_2\text{Mn}^{\text{IV}}(\text{bpy})_2$ Loaded into Cr-AIMCM-41, and 9.0 wt % $(\text{bpy})_2\text{Mn}^{\text{III}}(\mu\text{-O})_2\text{Mn}^{\text{IV}}(\text{bpy})_2$ Loaded into Cr-AIMCM-41

fit	sample, figure no.	shell	R (Å)	N (with $S_0^2 = 1.0$)	σ^2 ($\times 10^3 \text{Å}^2$) ^a	Φ ($\times 10^3$)	ϵ^2 ($\times 10^5$)
1	Cr-AIMCM, 4A	Cr–O	1.64	2.2	2	1.3	0.69
2	Mn_2 on Cr-AIMCM, 4C	Cr–O	1.64	1.7	2	0.9	0.47
3	Mn_2 max Cr-AIMCM, 4B	Cr–O	1.65	2.1	2	0.7	0.38
4	Cr-AIMCM, 4A	Cr–O	1.64	2.8	2	0.8	0.44
		Cr–O	1.87	1.1			
5	Mn_2 on Cr-AIMCM, 4C	Cr–O	1.65	2.0	2	0.6	0.34
		Cr–O	1.91	0.6			
6	Mn_2 max Cr-AIMCM, 4B	Cr–O	1.65	2.3	2	0.6	0.32
		Cr–O	1.89	0.5			

^a Values were fixed during minimization.

adsorbed onto the surface, but the complex is otherwise intact. EPR spectra confirm that no breakup of the dinuclear Mn core takes place upon loading onto the silica support. The $\text{Mn}^{\text{III}}(\mu\text{-O})_2\text{Mn}^{\text{IV}}$ oxidation state is manifested in the EPR spectrum by a characteristic 16-line signal, shown in Figure 3.²⁸ This signal does not significantly change when the complex is loaded into nanoporous silica, as described in more detail below.

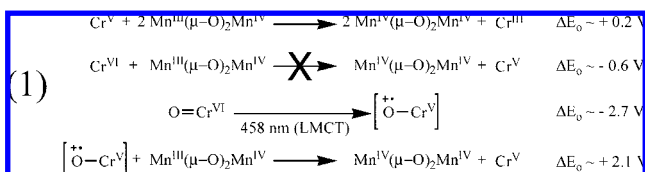
The ability of EPR spectroscopy to detect changes in $\text{Mn}^{\text{III}}(\mu\text{-O})_2\text{Mn}^{\text{IV}}$ structure on the surface allows us to determine the longer term stability of the complex loaded into AIMCM-41. As can be seen in Figure 4, we are able to observe the formation of Mn^{II} from $\text{Mn}^{\text{III}}(\mu\text{-O})_2\text{Mn}^{\text{IV}}$ over time, indicated by the appearance of its characteristic 6-line EPR signal. In the case of $(\text{terpy})\text{Mn}^{\text{III}}(\mu\text{-O})_2\text{Mn}^{\text{IV}}(\text{terpy})$, this reaction (presumably disproportionation) is observable

within hours of loading and is complete within a day when the sample is maintained under ambient conditions. When $(\text{bpy})_2\text{Mn}^{\text{III}}(\mu\text{-O})_2\text{Mn}^{\text{IV}}(\text{bpy})_2$ or $(\text{phen})_2\text{Mn}^{\text{III}}(\mu\text{-O})_2\text{Mn}^{\text{IV}}(\text{phen})_2$ is loaded, we find that they remain stable for significantly longer periods of time, the formation of Mn^{II} is only observable after 3 weeks and is complete after 2–3 months under identical conditions. This remarkable stability of $(\text{bpy})_2\text{Mn}^{\text{III}}(\mu\text{-O})_2\text{Mn}^{\text{IV}}(\text{bpy})_2$ within AIMCM-41 enables the detailed study of this system.

The FT of the Cr K-edge EXAFS (Figure 5(I)) shows the short (1.64 Å) Cr=O distance characteristic for tetrahedral Cr^{VI} centers anchored on the silica pore surface.²¹ The Cr K-edge EXAFS curve-fitting results are summarized in Table 2. The analysis reveals two peaks: one corresponds to the two Cr=O bonds, and the other indicates a longer Cr–O bond around 1.9 Å,^{21,25} in agreement with the expected $(\text{SiO})_2\text{Cr}(\text{O})_2$ structure of the site. The absence of an additional separate peak at ~ 2 Å

(28) Cooper, S. R.; Dismukes, G. C.; Klein, M. P.; Calvin, M. *J. Am. Chem. Soc.* **1978**, *100*, 7248–7252.

Scheme 1



indicates that reduction of Cr^{VI} (to Cr^{V}) is insignificant under these conditions,²¹ confirming that Cr^{VI} is the prevalent chromium species before and after loading of the dinuclear Mn complexes. This finding is consistent with Cr K-edge XANES (Figure 5(II)), which shows negligible effect on the intensity of the 1s-3d pre-edge peak of Cr^{VI} upon loading of the dinuclear Mn complex into Cr-AIMCM-41 (0.5 wt %); Figure 5(II), curve G shows the intense Cr K-edge XANES pre-edge peak of tetrahedral Cr^{VI} centers anchored on the silica pore surface. The band is characteristic for tetrahedrally coordinated Cr^{VI} but is absent for octahedral (centrosymmetric) Cr^{III} shown in curve D for the case of $\text{Cr}(\text{NO}_3)_3$, typical for such systems.²⁷ The Cr pre-edge peak intensity is decreased by at most 15% upon loading of the Mn complex (curve F) or bipyridyl ligand (curve E). Furthermore, no second nearest neighbor signal is observed in the FT of the Cr K-edge EXAFS (Figure 5(I)), indicating that the interaction of the Cr center with the Mn complex does not give rise to an ordered structure as one might expect for a covalent Cr–O–Mn linkage. The absence of second nearest neighbor peaks also rules out the presence of Cr oxide clusters in the Cr-AIMCM-41 samples, as these would give rise to Cr–Cr peaks.

While the Mn K-edge EXAFS and XANES data indicate a high degree of conservation of the di- μ -oxo structure of the $\text{Mn}(\mu\text{-O})_2\text{Mn}$ core upon loading of the complex onto the nanoporous silica support, the 16-line EPR signal allows us to evaluate the integrity of the $\text{Mn}^{\text{III}}\text{Mn}^{\text{IV}}$ oxidation state upon loading.²⁸ No shifts of the peak positions of the EPR hyperfine lines are noted for $(\text{bpy})_2\text{Mn}^{\text{III}}(\mu\text{-O})_2\text{Mn}^{\text{IV}}(\text{bpy})_2$ in solution (Figure 3, trace C), in Cr-AIMCM-41 (trace B), or in AIMCM-41 (trace A). This confirms that no significant structural changes of the $\text{Mn}^{\text{III}}\text{Mn}^{\text{IV}}$ core occur when loaded into the silica channels. Slight broadening of the hyperfine splitting is noted upon adsorption of the complex, reflecting both the increased disorder of the ligand environment (as observed by Mn K-edge XANES) and the increased anisotropy of the environment for complexes adsorbed on nanoporous surfaces.²⁹ Also, no effect of the Cr centers on the $\text{Mn}^{\text{III}}\text{Mn}^{\text{IV}}$ spectrum is detected. While the majority of the Cr centers in calcined Cr-AIMCM-41 (Cr/Si = 0.007) are Cr^{VI} , a small fraction of the centers are Cr^{V} ($g_{\perp} = 1.977$, $g_{\parallel} = 1.890$ in Figure 3 inset; the g_{\parallel} signal is obscured by the Mn 16-line signal in all other spectra).²¹ We have found that the Cr^{V} signal decreases linearly with increased loading of the dinuclear Mn complex, likely by spontaneous thermal oxidation of $\text{Mn}^{\text{III}}\text{Mn}^{\text{IV}}$ to $\text{Mn}^{\text{IV}}\text{Mn}^{\text{IV}}$ (Figure S1, Supporting Information). This is corroborated by the blue shift of the Mn K-edge XANES of $(\text{bpy})_2\text{Mn}^{\text{III}}(\mu\text{-O})_2\text{Mn}^{\text{IV}}(\text{bpy})_2$ in Cr-AIMCM-41 relative to AIMCM-41 (Figure 2(II), curves E and F); in higher oxidation states, the Mn K-edge XANES shift to higher energy.³⁰ The observation is in agreement with the

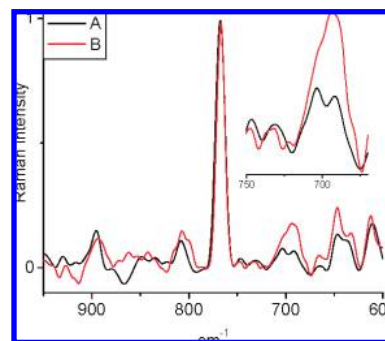


Figure 6. FT-Raman of $(\text{bpy})_2\text{Mn}^{\text{III}}(\mu\text{-O})_2\text{Mn}^{\text{IV}}(\text{bpy})_2$ loaded onto Cr-AIMCM-41 in different weight ratios: (A) 2.5 wt % and (B) 5.0 wt %. Spectra are normalized relative to the bipyridyl ligand absorption at 765 cm^{-1} . The inset expands the $\text{Mn}^{\text{III}}\text{Mn}^{\text{IV}}$ absorption at 700 cm^{-1} .

strong oxidizing power of Cr^{V} in solution ($E_0 = 1.34 \text{ V}$,³¹ compared to 1.16 V for $(\text{bpy})_2\text{Mn}^{\text{III}}(\mu\text{-O})_2\text{Mn}^{\text{IV}}(\text{bpy})_2$).³² Note that, by contrast, Cr^{VI} ($E_0 = 0.55 \text{ V}$ ³¹) is unable to spontaneously oxidize the dinuclear Mn complex to the $\text{Mn}^{\text{IV}}\text{Mn}^{\text{IV}}$ state, as seen in Scheme 1. Although the true potentials of these redox-active molecules on silica surfaces is not known, the solution measurements do allow for a correct prediction of the reactivity between these complexes. The presence of residual Cr^{V} at low loading levels also supports the idea that the dinuclear Mn complexes have limited mobility on the surface of AIMCM-41, as Cr^{V} would otherwise be titrated by excess $\text{Mn}^{\text{III}}\text{Mn}^{\text{IV}}$. Aside from this small effect of residual Cr^{V} on $\text{Mn}^{\text{III}}\text{Mn}^{\text{IV}}$ upon loading, the EPR spectra show that the concentration of $\text{Mn}^{\text{III}}\text{Mn}^{\text{IV}}$ species increases linearly with the amount of $(\text{bpy})_2\text{Mn}^{\text{III}}(\mu\text{-O})_2\text{Mn}^{\text{IV}}(\text{bpy})_2$ loaded into the nanoporous Cr-AIMCM-41 or AIMCM-41, up to the maximum loading ($\sim 9 \text{ wt } \%$).

The Mn–O stretch region of the FT-Raman spectrum allows us to simultaneously monitor the complex in the $\text{Mn}^{\text{III}}\text{Mn}^{\text{IV}}$ and the $\text{Mn}^{\text{IV}}\text{Mn}^{\text{IV}}$ oxidation states, in addition to observing possible effects of the loading on the bipyridyl ligand spectra. A comparison of spectra of the dinuclear Mn complex in Cr-AIMCM-41 at 2.5% and 5% loading is presented in Figure 6. Two bands show an approximate doubling of the intensity, namely one around 700 cm^{-1} and the other at 645 cm^{-1} . The 700 cm^{-1} feature is in the region where Mn–O modes of $\text{Mn}^{\text{III}}(\mu\text{-O})_2\text{Mn}^{\text{IV}}$ are expected to absorb, while a band in the $640 - 650 \text{ cm}^{-1}$ range is typical for Mn–O modes of $\text{Mn}^{\text{IV}}(\mu\text{-O})_2\text{Mn}^{\text{IV}}$.³³ On the basis of this comparison to literature values, we assign the 700 cm^{-1} band to $\text{Mn}^{\text{III}}(\mu\text{-O})_2\text{Mn}^{\text{IV}}$ and the absorption at 645 cm^{-1} to $\text{Mn}^{\text{IV}}(\mu\text{-O})_2\text{Mn}^{\text{IV}}$. Note that the 700 cm^{-1} region is free of any absorption of bipyridyl (isolated or bound to Mn), while the 645 cm^{-1} band is overlapped by a broad ligand absorption (Figures S2 and S5, Supporting Information). Hence, this pair of Raman bands, along with the Mn K-edge XANES results, allows us to qualitatively follow the relative abundance of oxidation states for the dinuclear Mn complex. Moreover, the 893 cm^{-1} band in the FT-Raman spectrum, originating from the symmetric $\text{O}=\text{Cr}^{\text{VI}}=\text{O}$ mode, allows us to simultaneously monitor the concentration of the Cr^{VI} species. Aside from these absorptions, all other bands in

(29) Lunina, E. V. *Appl. Spectrosc.* **1996**, *50*, 1413–1420.

(30) Yachandra, V. K.; Sauer, K.; Klein, M. P. *Chem. Rev.* **1996**, *96*, 2927–2950.

(31) Bard, A. J.; Parsons, R.; Jordan, J., Eds. *Standard Potentials in Aqueous Solution*; Marcel Dekker Inc.: New York, 1985.

(32) Collomb-Dunand-Sauthier, M.-N.; Deronzier, A.; Pradon, X.; Ménage, S.; Philouze, C. *J. Am. Chem. Soc.* **1997**, *119*, 3173–3174.

(33) Hasegawa, K.; Ono, T. *Bull. Chem. Soc. Jpn.* **2006**, *79*, 1025–1031.

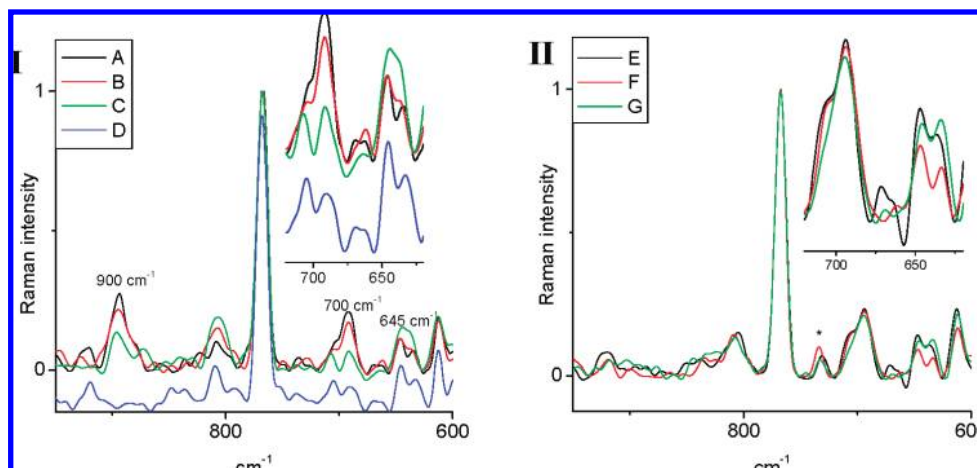


Figure 7. (I) FT-Raman spectra of Cr-AIMCM-41 loaded with 1.5 wt % $(\text{bpy})_2\text{Mn}^{\text{III}}(\mu\text{-O})_2\text{Mn}^{\text{IV}}(\text{bpy})_2$ which was illuminated with a 458 nm laser operating at 170 mW: (A) before illumination, (B) after illumination for 5 min, and (C) after illumination for 30 min. Spectrum (D) is for 0.5 wt % $(\text{bpy})_2\text{Mn}^{\text{III}}(\mu\text{-O})_2\text{Mn}^{\text{IV}}(\text{bpy})_2$ loaded in AIMCM-41. (II) The same photolysis experiment conducted with 1.5 wt % $(\text{bpy})_2\text{Mn}^{\text{III}}(\mu\text{-O})_2\text{Mn}^{\text{IV}}(\text{bpy})_2$ loaded onto AIMCM-41: (E) before illumination, (F) after illumination for 5 min, and (G) after illumination for 30 min. Asterisk denotes residual acetonitrile.

the FT-Raman spectrum are due to bipyridyl ligand absorptions. While there are small differences between the ligand spectrum of the crystalline Mn complex and the spectrum of the loaded complex, no significant effect of the presence of Cr on band frequencies or intensities is observed. Since the ligand is in large molar excess ($\text{bpy}:\text{Mn}_2 = 25:1$ in this system), this is to be expected.

In summary, the spectroscopic characterization of $(\text{bpy})_2\text{Mn}^{\text{III}}(\mu\text{-O})_2\text{Mn}^{\text{IV}}(\text{bpy})_2$ loaded into the channels of Cr-AIMCM-41 sieve reveals a material with the structure of the Mn complex completely intact and the oxidation state largely retained, and with almost all Cr centers in the oxidation state Cr^{VI} . The dominating driving forces for the adsorption of dinuclear Mn complexes into the silica nanopores are probably an as yet undefined combination of dispersion interactions, electrostatic binding, and H-bonding between the bpy ligands and the siloxane and surface silanol groups (as evidenced by the ease of adsorption of free bipyridine into AIMCM-41).

2.2. Light-Driven Oxidation of $\text{Mn}^{\text{III}}\text{Mn}^{\text{IV}}$ to $\text{Mn}^{\text{IV}}\text{Mn}^{\text{IV}}$ by Cr^{VI} Ligand-to-Metal Charge-Transfer (LMCT) Excitation. Upon illumination with visible light, samples of Cr-AIMCM-41 containing 1.5 wt % $(\text{bpy})_2\text{Mn}^{\text{III}}(\mu\text{-O})_2\text{Mn}^{\text{IV}}(\text{bpy})_2$ were found to have undergone the redox reaction $\text{Cr}^{\text{VI}} + \text{Mn}^{\text{III}}\text{Mn}^{\text{IV}} \rightarrow \text{Cr}^{\text{V}} + \text{Mn}^{\text{IV}}\text{Mn}^{\text{IV}}$, which is endoergic by 0.61 V.^{31,32} Each reactant and product redox state is observed upon illumination using a combination of EPR, XANES, and FT-Raman spectroscopy. As seen in Figure 7(I), the FT-Raman band of $(\text{Mn}^{\text{III}}(\mu\text{-O})_2\text{Mn}^{\text{IV}})$ at 700 cm^{-1} decreases during illumination; spectra following 5 min (trace B) and 30 min (trace C) irradiation at 458 nm (170 mW) are shown (see Supporting Information, Figure S7, for the DRS of these materials).²³ Note that the features around 700 cm^{-1} remaining after 30 min illumination are not noise but coincide with bands observed when $(\text{bpy})_2\text{Mn}^{\text{III}}(\mu\text{-O})_2\text{Mn}^{\text{IV}}(\text{bpy})_2$ is loaded into AIMCM-41 at low concentration (0.5 wt %, trace D). This shows that the $\text{Mn}^{\text{III}}\text{Mn}^{\text{IV}}$ complexes remaining after continued illumination occupy sites similar to those preferentially occupied at low loading levels. No visible light-induced depletion is observed for the complex in AIMCM-41 (free of Cr), as shown in Figure 7(II). This excludes the possibility of $\text{Mn}^{\text{III}}\text{Mn}^{\text{IV}}$ depletion through light absorption by the dinuclear Mn complex itself. In agreement with the Raman observations, EPR spectroscopy shows a decrease in intensity

for the 16-line signal of $\text{Mn}^{\text{III}}(\mu\text{-O})_2\text{Mn}^{\text{IV}}$ for the complex loaded into Cr-AIMCM-41 (Figure 8, spectra A and B) but no change for the complex loaded into AIMCM-41 (Figure 8, spectra C and D). We conclude that $\text{Mn}^{\text{III}}(\mu\text{-O})_2\text{Mn}^{\text{IV}}$ in Cr-AIMCM-41 is oxidized upon visible light excitation of the Cr^{VI} ligand-to-metal charge-transfer (LMCT) chromophore.

The product of this photooxidation is $\text{Mn}^{\text{IV}}(\mu\text{-O})_2\text{Mn}^{\text{IV}}$, as indicated by the increase of the band at 645 cm^{-1} in the FT-Raman spectrum.³³ While bpy ligand bands also absorb in this region (see Figures S2 and S5, Supporting Information), the increase in intensity upon illumination occurs only when both Cr^{VI} and $\text{Mn}^{\text{III}}(\mu\text{-O})_2\text{Mn}^{\text{IV}}$ are present. Assignment of the photoproduct to $\text{Mn}^{\text{IV}}(\mu\text{-O})_2\text{Mn}^{\text{IV}}$ is also supported by the observation that, upon disappearance of $\text{Mn}^{\text{III}}(\mu\text{-O})_2\text{Mn}^{\text{IV}}$, no other EPR-active Mn signal is observed. In particular, no Mn^{II} , a known disproportionation product of this type of complex³⁰ with its characteristic 6-line signal (Figure 4C), is formed. Since $\text{Mn}^{\text{IV}}(\mu\text{-O})_2\text{Mn}^{\text{IV}}$ is EPR silent, the absence of additional Mn signals upon illumination is consistent with the formation of $\text{Mn}^{\text{IV}}(\mu\text{-O})_2\text{Mn}^{\text{IV}}$. Furthermore, X-ray absorption spectra of samples of the dinuclear Mn complex on Cr-AIMCM-41 recorded before and after illumination exhibit an $\sim 1\text{ eV}$ shift of the Mn K-edge XANES second-derivative zero crossing point to higher energy (Figure 9(I)), which is characteristic for oxidation of the Mn center.²⁶

The decrease of the Cr^{VI} Raman mode at 895 cm^{-1} , assigned to the symmetric $\text{Cr}=\text{O}$ mode of tetrahedral Cr^{VI} ,²⁰ upon 458 nm irradiation (Figure 7(I)) and concurrent growth of the $g_{\perp} = 1.977$ EPR signal of Cr^{V} (Figure 8B) confirms that photooxidation of $\text{Mn}^{\text{III}}(\mu\text{-O})_2\text{Mn}^{\text{IV}}$ to $\text{Mn}^{\text{IV}}(\mu\text{-O})_2\text{Mn}^{\text{IV}}$ is accompanied by the reduction of Cr^{VI} to Cr^{V} (see Scheme 1). The corresponding bands are absent when the illumination is conducted with dinuclear Mn complexes loaded into AIMCM-41 (Figures 7(II) and 8D). The reduction of the Cr centers is further confirmed by a red shift of $\sim 1\text{ eV}$ in the Cr K-edge XANES second-derivative zero crossing point,²⁷ as shown in Figure 9(II). We conclude that photoexcitation of $\text{Cr}^{\text{VI}}\text{-O}$ LMCT induces electron transfer from $\text{Mn}^{\text{III}}(\mu\text{-O})_2\text{Mn}^{\text{IV}}$ to Cr^{VI} , resulting in the formation of $\text{Mn}^{\text{IV}}(\mu\text{-O})_2\text{Mn}^{\text{IV}}$ and Cr^{V} .

On the basis of the number of photons absorbed by Cr^{VI} LMCT at 458 nm and the number of $\text{Mn}^{\text{III}}(\mu\text{-O})_2\text{Mn}^{\text{IV}}$ complexes converted to $\text{Mn}^{\text{IV}}(\mu\text{-O})_2\text{Mn}^{\text{IV}}$, as determined by the

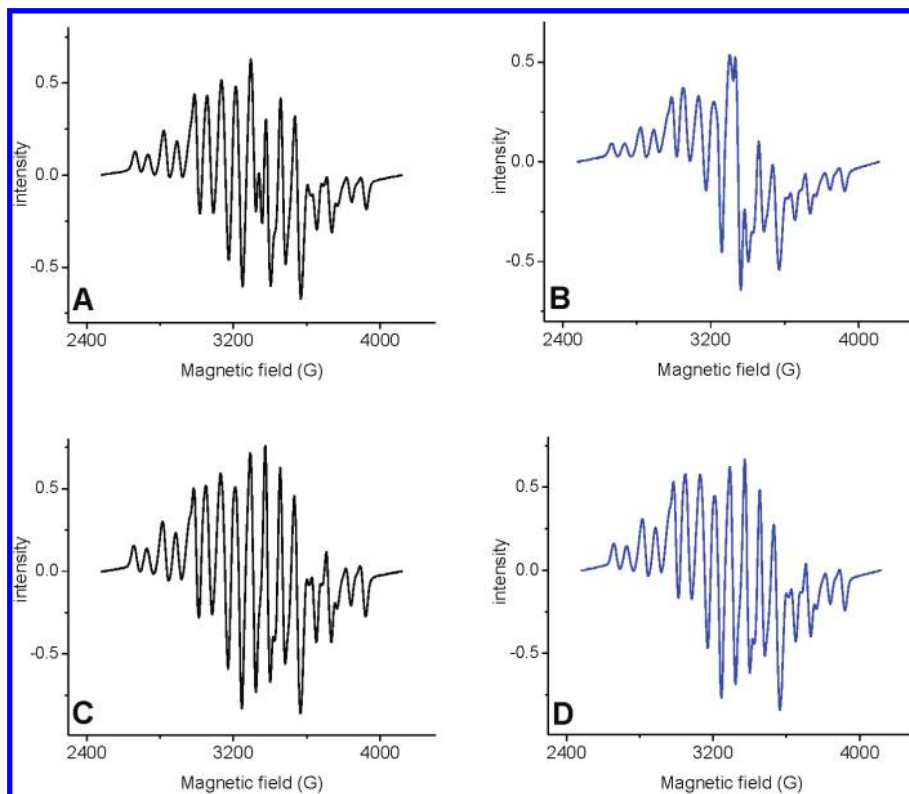


Figure 8. X-band EPR spectra of $(\text{bpy})_2\text{Mn}^{\text{III}}(\mu\text{-O})_2\text{Mn}^{\text{IV}}(\text{bpy})_2$ (1.5 wt %) on Cr-ALMCM-41 and ALMCM-41 illuminated at 458 nm: (A) before and (B) after 30 min illumination of complex in Cr-ALMCM-41; (C) before and (D) after 30 min illumination of complex in ALMCM-41. Spectra are from the same samples for which FT-Raman spectra are shown in Figure 6, traces A, C, E, and G, respectively. Spectra are normalized per milligram of material.

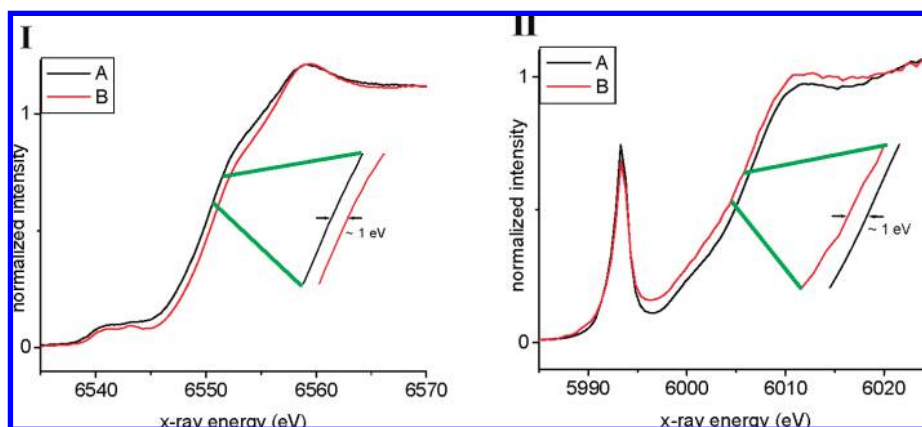


Figure 9. (I) Mn and (II) Cr K-edge XANES of $(\text{bpy})_2\text{Mn}^{\text{III}}(\mu\text{-O})_2\text{Mn}^{\text{IV}}(\text{bpy})_2$ (1.5 wt %) on Cr-ALMCM-41 before (trace A) and after (trace B) illumination with a 458 nm laser emission for 30 min.

decrease in the intensity of the 16-line EPR signal, a quantum efficiency of 10% was estimated for the light-induced electron transfer. (This constitutes a lower limit because it is assumed that each Cr^{VI} center in the silica material contributes to photon-induced electron transfer, which may not be the case.) The estimate shows that the uphill electron transfer, $\text{Cr}^{\text{VI}} + \text{Mn}_2^{\text{III,IV}} \rightarrow \text{Cr}^{\text{V}} + \text{Mn}_2^{\text{IV,IV}}$, with $\Delta E_o = -0.61$ V,^{31,32} results in a substantial fraction of the charge-separated products surviving on the time scale of minutes at room temperature. To our knowledge, this is the first observation of visible light-driven oxidation of a dinuclear Mn complex to the (IV,IV) oxidation state. The most likely origin of the long lifetime of the charge-separated products is hole hopping on intervening oxygen atoms: upon activation of the $\text{Cr}^{\text{VI}}\text{-O}$ ligand-to-metal charge-transfer

state to yield $\text{Cr}^{\text{V}}\text{-O}^{\bullet}$ (Scheme 1), the transient hole on O can hop to a neighboring O of the silica environment (i.e., $\text{Cr}\text{-O}^{\bullet}$ to $\text{Si}\text{-O}^{\bullet}$) before pulling an electron from a $\text{Mn}^{\text{III}}(\mu\text{-O})_2\text{Mn}^{\text{IV}}$ unit. For such a configuration, back electron transfer from Cr^{V} to the oxidized dinuclear Mn complex is expected to be slow due to the separation of the metal centers by $\text{Si}\text{-O}\text{-Si}$ surface groups. This result also suggests that the dinuclear Mn complexes are effectively immobile on the nanopore surfaces. There is very likely a distribution of lifetimes for the charge-separated products due to differences in the way dinuclear Mn complexes are arranged around Cr centers. Furthermore, a factor that may contribute to the long lifetime for charge separation is the large reorganization energy associated with Cr^{VI} to Cr^{V} reduction (replacement of the short $\text{Cr}=\text{O}$ double bond by the

0.4 Å longer Cr–O single bond),²¹ which will slow down back-reaction. Time-resolved optical studies of electron transfer between the dinuclear Mn complex and the Cr^{VI} chromophore are needed to obtain a complete overview of the electron-transfer processes and their kinetics. Such studies are in progress.

3. Conclusions

In summary, we have loaded transition metal di- μ -oxo dinuclear Mn complexes with bpy, phen, or terpy ligands into nanoporous silica materials. The complex with bpy ligands exhibited by far the best stability. FT-Raman, EXAFS, XANES, and EPR spectroscopy confirmed that (bpy)₂Mn^{III}(μ -O)₂Mn^{IV}(bpy)₂ retains its structural integrity inside the nanoscale silica channels for weeks at room temperature. Moreover, the majority of the (bpy)₂Mn(μ -O)₂Mn(bpy)₂ complexes remain in the (III,IV) oxidation state upon loading; no Mn^{II}-containing decomposition products were observed. Excitation of the Cr^{VI}–O LMCT absorption with visible light results in the oxidation of the dinuclear Mn^{III}(μ -O)₂Mn^{IV} state to Mn^{IV}(μ -O)₂Mn^{IV}, with all initial and final states of the electron transfer spectroscopically identified. The charge separation products were found to last up to several minutes at room temperature. Charge transport from the Cr–O sites to the dinuclear Mn complexes by hole hopping is thought to be primarily responsible for the long lifetime of the charge separation because it allows for significant spatial separation of the Cr and Mn centers.

With this direct spectroscopic observation of visible light-driven oxidation of a complex relevant to water oxidation by a metal center chromophore in silica nanopores, we are able to begin studying the detailed energetics and kinetics of photon-induced electron flow between multi-electron-transfer catalysts and molecular charge-transfer chromophores inside high-surface-area oxide supports. A complete assessment of the electron-transfer processes of the photocatalytic units requires time-resolved monitoring of the various spectra, which will become particularly important as the single Cr LMCT center is replaced by a heterodinuclear charge-transfer chromophore with a donor potential that can be tuned or selected.²¹

4. Experimental Section

Unless otherwise noted, all manipulations were carried out under ambient conditions with solvents and materials used as received from the manufacturer.

Synthesis of Di- μ -oxo Dinuclear Mn Complexes. [bpy₄Mn₂(μ -O)₂][BF₄]₃,³⁴ [phen₄Mn₂(μ -O)₂][BF₄]₃,³⁵ and [terpy₂Mn₂(μ -O)₂(H₂O)₂][NO₃]₃^{36,37} were synthesized by literature methods or small variations thereof.

Synthesis of Cr-AIMCM-41 and AIMCM-41. Cr-AIMCM-41 was synthesized via hydrothermal synthesis as previously described.²⁴ Briefly, a solution of diethylamine (10 mL), 25 wt % cetyl trimethylammonium chloride (7.2 mL), and Al(NO₃)₃·9H₂O (0.6 g) in H₂O (65 mL) was prepared. A separate solution of Cr(NO₃)₃·9H₂O (0.065 g) in 25 wt % NH₄OH (3.6 mL) was sonicated for 30 min. The two solutions were combined and stirred for 30 min. Tetraethylorthosilicate (8.9 mL) was then added dropwise, resulting in a white slurry that was stirred for 4 h. This

mixture was transferred into a Parr bomb, sealed, and heated at 110 °C for 3 days. The resulting light blue solid was collected via filtration, washed with copious amounts of water, and dried at 100 °C for 6 h. This was followed by calcination at 630 °C for 6 h under air flow (1 °C/min ramp), resulting in a light yellow product. EPR spectroscopy revealed residual Cr^V not exceeding 5% (ref 21, Figure 4A, spectrum a). These centers are most likely in the interior of the silica walls separating the nanoscale channels and, hence, not reachable by oxygen. AIMCM-41 was synthesized by omitting Cr(NO₃)₃ from the above preparation. These materials were identical by IR, FT-Raman, and DRS to samples previously prepared in our laboratory.²⁴

Loading bpy₄Mn₂(μ -O)₂ into AIMCM-41. AIMCM-41 (100 mg) was placed in 10 mL of acetonitrile buffered with 0.01 M 2,2'-bipyridine (0.01 M bpy buffer) with vigorous stirring to form a slurry. Separately, a stock solution containing 1 mM (~1 mg/mL) [bpy₄Mn₂(μ -O)₂][BF₄]₃ in 0.01 M bpy buffer was prepared. The buffer is necessary as, according to our experience, [bpy₄Mn₂(μ -O)₂][BF₄]₃ slowly decomposes to form a brown solid in pure acetonitrile.³²

Depending on the amount of bpy₄Mn₂(μ -O)₂ loaded in the material, an appropriate amount of the stock solution was added dropwise into the AIMCM-41 slurry and allowed to stir for 1 h. The solid was then filtered, washed with 5 × 20 mL of acetonitrile, and dried *in vacuo* for 2 h. The final solid typically has no residual CH₃CN by FT-Raman and FT-IR. These materials were characterized by FT-Raman, EPR, TGA, DRS, and ICP-MS. Identical procedures were used to load bpy₄Mn₂(μ -O)₂ into Cr-AIMCM-41.

Loading phen₄Mn₂(μ -O)₂ into AIMCM-41. Samples were prepared similarly to bpy₄Mn₂(μ -O)₂-loaded materials, substituting [phen₄Mn₂(μ -O)₂][BF₄]₃ and 0.01 M 1,10-phenanthroline in acetonitrile (0.01 M phen buffer). These materials were characterized by EPR and FT-Raman. Although EPR demonstrated that Mn^{III}(μ -O)₂Mn^{IV} was loaded, we were unable to identify a strong characteristic FT-Raman signal for further study. This is due to ligand bands that overlap the area of interest. See Supporting Information for further characterization of this material (Figures S17 and S18).

Loading terpy₂Mn₂(μ -O)₂ into AIMCM-41. The samples were manipulated similarly to other materials of this type. The loading solution was prepared from a methanol solution of [terpy₂Mn₂(μ -O)₂][NO₃]₃ (1 mM) and an appropriate amount added to a separate slurry of 100 mg of AIMCM-41 in 10 mL of methanol and stirred for 1 h. The resulting solid was filtered, washed with methanol (5 × 20 mL), and dried *in vacuo*. The material was characterized by EPR and FT-Raman. While EPR of immediately frozen (liquid N₂) materials showed that Mn^{III}(μ -O)₂Mn^{IV} was successfully loaded into AIMCM-41, no strong characteristic FT-Raman signals could be observed for Mn^{III}(μ -O)₂Mn^{IV}. This could be due to the instability of terpy₂Mn₂^{III/IV}O₂ within AIMCM-41 (Figure 4) or overlapping ligand absorptions in the region of interest. See Supporting Information (Figure S16) for more details on this material.

Determining Maximum Load of L₄Mn₂(μ -O)₂ into AIMCM-41. A 1 mM solution of [L₄Mn₂(μ -O)₂][BF₄]₃ (L = bpy, phen) in 0.01 M acetonitrile was prepared. This was then added in differing amounts to approximately 30 mg of AIMCM-41, resulting in final loading levels between 10 and 15 wt %. For instance, 3.5 mL of a 1 mM stock solution was added to 27.8 mg of AIMCM-41, resulting in a maximum possible load of 12.3 wt %. This solution was stirred for 1 h and then filtered to collect the supernatant. The supernatant was compared to the remaining stock solution by UV/vis spectroscopy. The amount of [L₄Mn₂(μ -O)₂][BF₄]₃ remaining in solution after loading was measured by comparing four points (450, 530, 600, and 690 nm) before and after the loading procedure. Each material combination was measured at three loading levels (typically 10, 12, and 15 wt %), with the results combined to provide the values shown in Table S2 in the Supporting Information. The bpy₄Mn₂(μ -O)₂ system has slightly higher maximum loading than

(34) Cooper, S. R.; Calvin, M. *J. Am. Chem. Soc.* **1977**, *99*, 6623–6630. NaBF₄ is substituted for NaClO₄ in the synthesis.

(35) Morrison, M. M.; Sawyer, D. T. *J. Am. Chem. Soc.* **1977**, *99*, 257–258. NaBF₄ is substituted for NaClO₄ in the synthesis.

(36) Limburg, J.; Vrettos, J. S.; Liabre-Sands, L. M.; Rheingold, A. L.; Crabtree, R. H.; Brudvig, G. W. *Science* **1999**, *283*, 1524–1527.

(37) Collomb, M.-N.; Deronzier, A.; Richardot, A.; Décant, J. *New J. Chem.* **1999**, *23*, 351–353.

phen₄Mn₂(μ-O)₂ (~9:7.5 wt %). There was no significant difference between loading on AlMCM-41 and Cr-AlMCM-41 in either system.

FT-Raman Sample Preparation and Data Acquisition. Samples were prepared by pressing approximately 1 mg of material into an aluminum sample well. Spectra were collected on a Bruker model IFS66 spectrometer with a FT-Raman module FRA-106 fitted with a liquid N₂-cooled Ge detector. Samples were typically illuminated with 1064 nm laser probe light at 300 mW, with 1000 scans recorded per sample.

EPR Analysis of Mn Containing Cr-AlMCM-41 and AlMCM-41. X-band EPR spectroscopy was performed with a Varian E-109 spectrometer, a standard TE₁₀₂ cavity, and an Air Products liquid helium cryostat. EPR spectra were typically collected at 20 K using 1 mW microwave power and 32 G modulation amplitude. Samples were prepared by lightly crushing the material, followed by placing it into a tared quartz EPR tube which was then sealed.

EXAFS Data Collection. X-ray absorption spectra were collected at the Stanford Synchrotron Radiation Laboratory (SSRL) on beamline 7-3 at electron energy 3.0 GeV and an average current 100–500 mA. The beamline is equipped with a Si(220) double crystal monochromator. The intensity of the incident X-rays was monitored by a N₂-filled ion chamber (*I*₀) in front of the sample. To reduce the sample damage by radiation, the incident X-ray beam was defocused at the sample position. The samples were protected from the beam during spectrometer movements between different energy positions by a shutter synchronized with the scan program. The samples were kept at 9 ± 1 K in a He atmosphere at ambient pressure using an Oxford CF-1208 continuous-flow liquid He cryostat. Data were recorded as fluorescence excitation spectra using a germanium 30-element energy-resolving detector (Canberra Electronics). For Mn K-edge XAS, energy was calibrated by the pre-edge peak of KMnO₄ (6543.3 eV), which was placed between two N₂-filled ionization chambers (*I*₁ and *I*₂) after the sample. For Cr K-edge XAS, Cr foil was used with *E*₀ = 5989.0 eV, corresponding to the first peak of the first derivative on the Cr⁰ edge.

EXAFS Data Analysis. Data reduction has been described previously³⁸ and is described in more details in the Supporting Information (Figures S3 and S4).

Stability of Loaded L_xMn₂(μ-O)₂ AlMCM-41 Materials. Samples were stored under air at room temperature and periodically removed for EPR and FT-Raman analysis. In the case of terpy₂Mn₂O₂ loaded materials, the initial samples were immediately

frozen under liquid nitrogen after the loading procedure was completed for EPR and FT-Raman analysis. It was found that L₄Mn₂(μ-O)₂ (L = bpy, phen) were stable for weeks to months under ambient conditions, while terpy₂Mn₂(μ-O)₂ samples were stable for only a few hours, forming unidentified Mn^{II} products (see Figure 4). EPR shows that a similar Mn^{II} product is the final result for all AlMCM-41 material containing L_xMn₂(μ-O)₂ cores.

Illumination of Cr-AlMCM-41 and AlMCM-41 Containing bpy₄Mn₂(μ-O)₂. Samples were prepared by pressing ~5 mg of material into a pellet 1 cm in diameter using 2 tons of force. The pellet was placed in a stainless steel IR vacuum cell equipped with CaF₂ or KBr windows. Samples in the evacuated cell were illuminated with 458 nm Ar ion laser emission at 170 mW, with the beam expanded to 1 cm to cover the entire sample pellet. At time intervals between 0 (control) and 30 min, samples were removed from the beam for analysis by FT-Raman or EPR. For EPR measurements, the pellet was crushed, placed in quartz EPR tubes, and stored under liquid N₂ if there was a time lag between illumination and recording of spectra.

Acknowledgment. This work was supported by the Director, Office of Science, Office of Basic Energy Sciences, Division of Chemical Sciences, Geosciences and Biosciences of the U.S. Department of Energy under Contract DE-AC03-76SF00098. Portions of this research were carried out at the Stanford Synchrotron Radiation Laboratory, a national user facility operated by Stanford University on behalf of the U.S. Department of Energy, Office of Basic Energy Sciences. The SSRL Structural Molecular Biology Program is supported by the Department of Energy, Office of Biological and Environmental Research, and by the National Institutes of Health, National Center for Research Resources, Biomedical Technology Program. We thank Dr. Junko Yano (LBNL) for discussions regarding the analysis and interpretation of the EPR and X-ray spectroscopy data and for her contributions to the collection of these data. The compound (Me₂-bpy)₂Mn^{IV}(μ-O)₂Mn^{IV}(Me₂bpy)₂ was provided by William Armstrong and Sumitra Mukerji (BC).

Supporting Information Available: Complete FT-Raman spectra of bpy₄Mn₂O₂, phen₄Mn₂O₂, terpy₂Mn₂O₂, and AlMCM-41 loaded materials; *k*-space and fitting parameters of EXAFS; full EPR, DRS, TGA, and maximum loading calculations for bpy₄Mn₂O₂. This material is available free of charge via the Internet at <http://pubs.acs.org>.

JA801546A

(38) Robblee, J. H.; Messinger, J.; Cinco, R. M.; McFarlane, K. L.; Fernandez, C.; Pizarro, S. A.; Sauer, K.; Yachandra, V. K. *J. Am. Chem. Soc.* **2002**, *124*, 7459–7471.